

# HuGDiffusion: Generalizable Single-Image Human Rendering via 3D Gaussian Diffusion

Yingzhi Tang, Qijian Zhang, and Junhui Hou

**Abstract**—We present HuGDiffusion, a generalizable 3D Gaussian splatting (3DGS) learning pipeline to achieve novel view synthesis (NVS) of human characters from single-view input images. Existing approaches typically require monocular videos or calibrated multi-view images as inputs, whose applicability could be weakened in real-world scenarios with arbitrary and/or unknown camera poses. In this paper, we aim to generate the set of 3DGS attributes via a diffusion-based framework conditioned on human priors extracted from a single image. Specifically, we begin with carefully integrated human-centric feature extraction procedures to deduce informative conditioning signals. Based on our empirical observations that jointly learning the whole 3DGS attributes is challenging to optimize, we design a multi-stage generation strategy to obtain different types of 3DGS attributes. To facilitate the training process, we investigate constructing proxy ground-truth 3D Gaussian attributes as high-quality attribute-level supervision signals. Through extensive experiments, our HuGDiffusion shows significant performance improvements over the state-of-the-art methods. *Our code will be made publicly available.*

**Index Terms**—Human Digitization, Novel View Synthesis, Neural Rendering, 3D Gaussian Splatting, Diffusion Model

## I. INTRODUCTION

THREE-dimensional (3D) human digitization from single-view images has gained significant attention due to its wide-ranging applications in game production, filmmaking, immersive telepresence, and augmented/virtual reality (AR/VR). Recent advancements have led to the development of numerous methods leveraging deep learning architectures to infer 3D human from 2D image observations [33].

In terms of different learning objectives, existing 3D human digitization frameworks can be broadly categorized into two groups. *Reconstruction-oriented* approaches [6], [29], [45], [46] focus on recovering accurate 3D surface geometries of human characters while capturing corresponding appearance details, explicitly producing textured mesh models. However, these reconstructed meshes often suffer from issues such as incorrect poses, degenerate limbs, and overly smoothed surfaces. In contrast, *rendering-oriented* approaches [9], [36] prioritize visual presentation by synthesizing novel views from observed images, emphasizing rendering quality over precise geometric accuracy.

This work was supported in part by the NSFC Excellent Young Scientists Fund 62422118, and in part by the Hong Kong Research Grants Council under Grants 11219324, 11202320, and 11219422.

Yingzhi Tang and Junhui Hou are with the Department of Computer Science, City University of Hong Kong, Hong Kong SAR. E-mail: yztang4-c@my.cityu.edu.hk; jh.hou@cityu.edu.hk.

Qijian Zhang is with the TiMi L1 Studio of Tencent Games, China. Email: keeganzhang@tencent.com.

For human NVS, the primary objective is achieving high visual fidelity in rendered 2D images, irrespective of the accuracy of the underlying 3D geometric shapes. Most existing methods rely on video frame sequences or calibrated multi-view images as inputs, limiting their applicability in real-world scenarios with sparse views and unknown camera poses. To address this limitation, SHERF [8] introduce a generalizable NeRF [19]-based learning framework for single-view human NVS in a feed-forward manner. However, the differentiable volume rendering technique used in SHERF necessitates a large number of query points along ray directions to render specific pixels, significantly reducing the efficiency of both training and inference processes.

More recently, 3DGS [11] rapidly evolve as a flexible and efficient neural rendering component. Inheriting the learning paradigms of generalizable NeRF frameworks [2], [8], [41], the latest works [48], [52] build generalizable 3DGS frameworks by training a parameterized neural model to generate the desired set of Gaussian attributes, which can be further rendered through splat rasterization. Technically, building a generalizable human 3DGS learning framework for single-view NVS faces several major aspects of challenges:

- 1) inferring complete 3D human appearance from a single 2D image is inherently a conditional generation task that requires the generation of invisible parts based solely on information from the visible view. Regression-based models lack the capability to predict accurate appearances in occluded areas, necessitating a more robust generation mechanism;
- 2) the prevailing training paradigm relies on regression models supervised by pixel-level signals (see Fig. 1(a)). However, such signals are insufficient for training advanced generative models, such as diffusion models, highlighting the need for novel and more effective training signals;
- 3) single-view images lack crucial features such as 3D human structure and unseen clothing details, making model training challenging. Human-centric conditions are necessary to bridge these gaps.

To address these challenges, we propose a series of targeted solutions. We harness the diffusion mechanism to tackle this single-view human NVS as a conditional generation task (see Fig. 1(b)). Specifically, we design a diffusion-based framework named HugDiffusion, which comprises two core modules. The initial module leverages a human reconstruction pipeline to generate point clouds, which are then initialized as 3D Gaussian positions. In the second module, we propose a con-

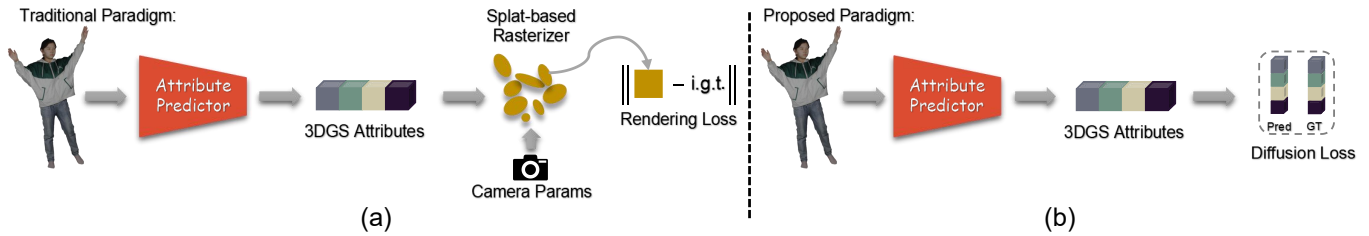


Fig. 1: (a) The traditional paradigm uses a splat-based rasterizer to supervise training with image signals. (b) HugDiffusion trains a diffusion model with 3D Gaussian attributes as supervision signals.

ditional Gaussian attribute diffusion module to learn the data distribution of 3D Gaussian attributes, enabling the generation of realistic and plausible results.

To facilitate the training process of the diffusion model, we customize a two-stage workflow to pre-create 3D Gaussian attribute sets as attribute-level supervision signals. The workflow comprises a per-scene overfitting stage and a distribution unification stage. This workflow leverages point cloud transformers to learn structured 3D Gaussians and align attribute distributions across diverse scenes.

Additionally, human-centric conditions are constructed by integrating SMPL-Semantic features and Pixel-Aligned features based on the 3D Gaussian positions. These conditions provide essential context for accurate reconstruction.

In summary, our main technical contributions are:

- we investigate a conditional diffusion framework for the generation of 3D Gaussian attribute sets, showing better generation capabilities than straightforward regression architectures;
- we propose a two-stage proxy ground-truth creation approach to achieve 3D Gaussian attribute sets as attribute-level supervision signals for the diffusion training process; and
- we develop a powerful human image feature extraction workflow, which effectively integrates human priors to extract more informative human-centric features to facilitate our conditional diffusion mechanism.

The remainder of this paper is organized as follows. Section II provides a comprehensive review of the existing literature, including human reconstruction methods, novel view synthesis methods, and diffusion models. Section III introduces our proposed two-stage proxy ground-truth construction process and HugDiffusion in detail. In Section IV, we analyze the necessity of the proxy ground-truth construction process and conduct extensive experiments and ablation studies to validate the effectiveness of HuGDiffusion. Finally, Section V concludes this paper.

## II. RELATED WORK

### A. Human Reconstruction

The geometry of the human body serves as a fundamental basis for achieving accurate novel view synthesis. Various 3D representations, such as voxels, point clouds, meshes, and implicit functions, have been explored to represent human anatomy. Among these, implicit functions have emerged as

a dominant approach for reconstructing geometric surfaces of the human body. PIFu and PIFuHD [29], [30] pioneered the use of implicit functions for monocular and multi-view human body reconstruction by predicting occupancy values of spatial points and extracting surfaces using the marching cubes algorithm. However, relying solely on image features without incorporating human body priors poses challenges in handling occluded regions.

To address this limitation, PAMIR and ICON [37], [49] integrated the parametric human model SMPL to enable implicit functions to better comprehend human body structure. Zhang et al. [45] further advanced the field by utilizing triplane representation and transformers to address issues such as loose clothing. SiFU [46] employed a text-to-image diffusion model to infer invisible details and produce realistic results. Despite these innovations, the reliance on SMPL introduces dependencies on accurate parameter estimation, as highlighted by Tang et al. [32], who demonstrated the challenges of refining SMPL parameters within implicit fields. Moreover, these methods often require querying a large number of spatial points to reconstruct 3D surfaces, which can be computationally intensive.

In contrast, HaP [32], a purely explicit method, represents the human body as a point cloud in 3D space, offering greater flexibility for modeling arbitrarily clothed human shapes with unconstrained topology. Due to its efficiency and adaptability, this work adopts HaP to generate 3D Gaussian positions.

### B. Novel View Synthesis

View synthesis remains an open challenge in both academic research and industry applications. Recently, implicit neural radiance representation (NeRF) [19] has achieved remarkable success in generating high-quality novel views. Numerous NeRF-based methods have since been proposed to address various tasks, including single-view human NeRF [8], [36] and multi-view human NeRF [2], [20]. By incorporating the parametric human model SMPL, NeRF-based methods [10], [38] eliminate the need for ground-truth 3D geometry and enable the rendering of high-quality human views. NeuralBody [23] introduced the use of NeRF for human novel view synthesis by learning structured latent codes for the canonical SMPL model across frames. HumanNerf [36] enhanced NeRF representations in canonical space by disentangling rigid skeleton motion from non-rigid clothing motion in monocular videos. Zhao et al. [47] and Gao et al. [2] projected SMPL

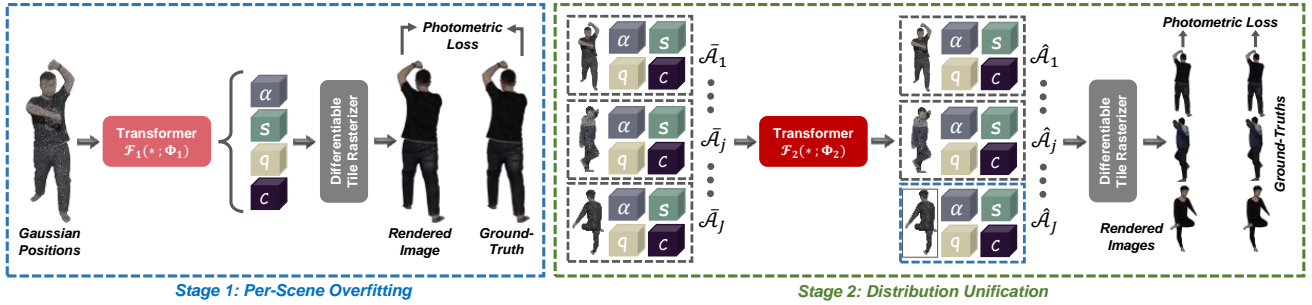


Fig. 2: The two-stage workflow of creating proxy ground-truth Gaussian attributes.

models onto multi-view images, combining image features with canonical SMPL features to create generalizable human NeRFs. SHERF [8] introduced a hierarchical feature map for generalizable single-view human NeRF. These generalizable methods typically follow the training paradigm of PixelNeRF [41].

Recently, efforts have shifted toward generalizable 3D Gaussian splatting (3DGS) models [14], [31], [35], [48], [52], which offer faster training and inference compared to NeRF. Some video-based methods [9], [12] focus on learning 3D Gaussian attributes in canonical space for rapid rendering, but they typically rely on monocular or multi-view videos and lack generalizability across scenes. Zou et al. [52] combined triplane and 3DGS representations, employing PIFu-like pixel-aligned features to train a generalizable 3DGS model. Zheng et al. [48] proposed a framework for multi-view human novel view synthesis that integrates iterative depth estimation and Gaussian parameter regression.

Another emerging category of methods [13], [39], [40] leverages the generative capabilities of large models [27] to predict unseen views. Tang et al. [31] and Xue et al. [39] combined diffusion-generated multi-view images with 3D information to generate 3D Gaussians. MagicMan [4] finetuned a stable diffusion model on human images and estimated SMPL models to synthesize novel human views. Similarly, our method utilizes a stable diffusion model [1] to infer unseen areas of a given human.

In this paper, a diffusion model is trained to predict 3D Gaussian distributions of the human body for novel view synthesis, employing attribute-level signals rather than pixel-level signals.

### C. Diffusion Models

Diffusion models are particularly suited for addressing monocular human rendering tasks due to their strong capability to model 3D Gaussian attribute distributions from single-view images. These models have demonstrated remarkable success across various domains, including text-to-image generation [27], [44], super-resolution [28], and low-light enhancement [7]. Since 3D Gaussians can be conceptualized as point clouds with attributes, we briefly review advancements in point cloud diffusion models.

Luo et al. [15] pioneered the use of diffusion models for point cloud generation. Zhou et al. [51] extended this idea by developing a conditioned diffusion model based on partial

point clouds. PDR [16] utilized a two-branch PointNet++ [24] architecture to train a diffusion model for point cloud completion. Additionally, several methods [17], [34] have explored training point cloud diffusion models in latent spaces. However, these approaches are primarily focused on generating point cloud positions and are not directly applicable to the diffusion of 3D Gaussian attributes. Among existing models, PC<sup>2</sup> [18] is notable for being a point cloud diffusion model conditioned on single-view images, generating point clouds with color attributes. However, PC<sup>2</sup> does not integrate human body priors, which limits its ability to handle human-centric scenarios effectively.

Efforts have also been made to train 3D Gaussian splatting (3DGS) diffusion models. For instance, GaussianCube [43] and L3DG [26] construct voxel-based 3DGS representations and employ 3D U-Net architectures for training diffusion models. DiffGS [50] adopts a different strategy by learning the diffusion model within implicit fields. Despite their innovations, these methods primarily target generative tasks and often struggle to recover fine details from conditioning images [43].

To address these limitations, we propose a tailored framework named HuGDiffusion, which leverages PointNet++ as its backbone. The framework incorporates meticulously designed human-centric conditioning mechanisms to enable effective diffusion of 3D Gaussian attributes, bridging the gap between generative capabilities and detailed reconstruction from single-view images.

## III. PROPOSED METHOD

### A. Preliminary of 3DGS

Different from implicit neural representation approaches [19], [21], 3DGS [11] explicitly encodes a radiance field as an unordered set of Gaussian primitives denoted as  $\mathcal{A} = \{\mathbf{a}^{(n)}\}_{n=1}^N$ . Each primitive is associated with a set of optimizable attributes:

$$\mathbf{a}^{(n)} = \{\mathbf{p}^{(n)}, \alpha^{(n)}, \mathbf{s}^{(n)}, \mathbf{q}^{(n)}, \mathbf{c}^{(n)}\}, \quad (1)$$

including position  $\mathbf{p}^{(n)} \in \mathbb{R}^3$ , opacity value  $\alpha^{(n)} \in \mathbb{R}$ , scaling factor  $\mathbf{s}^{(n)} \in \mathbb{R}^3$ , rotation quaternion  $\mathbf{q}^{(n)} \in \mathbb{R}^4$ , and spherical harmonics (SH) coefficients  $\mathbf{c}^{(n)} \in \mathbb{R}^d$ . For an arbitrary viewpoint with camera parameters  $\mathcal{V}$ , a differentiable tile rasterizer  $\mathcal{R}$  is applied to render the Gaussian attribute

set  $\mathcal{A}$  into the corresponding view image  $\mathbf{I}_r$ , which can be formulated as:

$$\mathbf{I}_r = \mathcal{R}(\mathcal{A}; \mathcal{V}). \quad (2)$$

For a set of observed  $K$  multi-view images  $\{\mathbf{I}^{(k)}\}_{k=1}^K$  depicting a specific scene, together with their calibrated camera parameters  $\{\mathcal{V}^{(k)}\}_{k=1}^K$ , the optimization process iteratively updates the Gaussian attributes by comparing the difference between rendered images and observed ground-truths, which can be formulated as:

$$\mathbf{I}_r^{(k)} = \mathcal{R}(\mathcal{A}; \mathcal{V}^{(k)}), \quad \min_{\mathcal{A}} \sum_{k=1}^K \ell_{\text{pmet}}(\mathbf{I}_r^{(k)}, \mathbf{I}^{(k)}), \quad (3)$$

where  $\ell_{\text{pmet}}(\cdot, \cdot)$  computes the pixel-wise photometric error within the image domain. After training, the resulting optimized Gaussian attribute set  $\mathcal{A}$  serves as a high-accuracy neural representation of the target scene for real-time NVS. However, despite the fast inference speed of 3DGS, scene-specific overfitting still requires at least several minutes to complete.

### B. Training Paradigm of Generalizable Feed-Forward 3DGS

In contrast to the conventional working mode of per-scene overfitting, many recent studies are devoted to constructing generalizable 3DGS frameworks [14], [31], [35], [48], [52] via shifting the actual optimization target from the Gaussian attribute set to a separately parameterized learning model  $\mathcal{M}(*; \Theta)$ , where  $*$  denotes network inputs and  $\Theta$  denotes network parameters. Generally, we can summarize that all such approaches uniformly share the same training paradigm, where the learning model  $\mathcal{M}(\cdot, \cdot)$  consumes its input to generate scene-specific Gaussian attributes at the output end. Through differentiable rendering  $\mathcal{R}$ , these approaches impose **pixel-level supervision** with image signals, as formulated below:

$$\min_{\Theta} \sum_{k=1}^K \ell_{\text{pmet}}(\mathcal{R}(\mathcal{M}(*; \Theta); \mathcal{V}^{(k)}), \mathbf{I}^{(k)}). \quad (4)$$

Although such a training paradigm is reasonable and straightforward, its reliance on regression-based supervision limits the model's ability to accurately generate appearances in some occluded regions.

To overcome this limitation, we propose a paradigm shift by introducing **attribute-level supervision**, enabling the effective training of diffusion-based models, which are well-known for their superior generative capabilities. Under our targeted setting with single-view image  $\mathbf{I}_s$  as input, the proposed training paradigm can be formulated as:

$$\mathcal{A} = \mathcal{M}(\mathbf{I}_s; \Theta), \quad \min_{\Theta} \ell_{\text{setdiff}}(\mathcal{A}, \hat{\mathcal{A}}), \quad (5)$$

where  $\ell_{\text{setdiff}}(\cdot, \cdot)$  measures the primitive difference between the predicted Gaussian attribute set  $\mathcal{A}$  and the pre-created proxy ground-truth attribute set  $\hat{\mathcal{A}}$ .

Overall, our proposed single-view generalizable human 3DGS learning framework consists of two core processing phases: 1) *creating proxy ground-truth Gaussian attributes as supervision signals*, and 2) *training a conditional diffusion model for Gaussian attribute generation*, as introduced in the following Sections III-C and III-D.

### C. Creation of Attribute-Level Signals

To facilitate attribute-level optimization, we need to pre-create a dataset of proxy ground-truth Gaussian attribute sets serving as the actual supervision signals for training  $\mathcal{M}$ . Formally, suppose that our raw training dataset is composed of  $J$  different human captures each associated with multi-view image observations  $\{\mathbf{I}_j^{(k)}\}_{k=1}^K$  and camera parameters  $\{\mathcal{V}_j^{(k)}\}_{k=1}^K$ , we aim to produce the corresponding proxy ground-truths  $\{\hat{\mathcal{A}}_j\}_{j=1}^J$  as:

$$\hat{\mathcal{A}}_j = \{\hat{\mathbf{a}}_j^{(n)}\}_{n=1}^N = \{\hat{\mathbf{p}}_j^{(n)}, \hat{\alpha}_j^{(n)}, \hat{\mathbf{s}}_j^{(n)}, \hat{\mathbf{q}}_j^{(n)}, \hat{\mathbf{c}}_j^{(n)}\}. \quad (6)$$

In fact, the most straightforward way of obtaining  $\{\hat{\mathcal{A}}_j\}_{j=1}^J$  is to separately overfit the vanilla 3DGS over each of the  $J$  human captures and save the resulting Gaussian attributes. Unfortunately, owing to the inevitable randomness of gradient-based optimization and primitive manipulation, the overall distributions of the independently optimized Gaussian attribute sets are typically inconsistent. Even for the same scene, two different runs produce varying Gaussian attribute sets (e.g., primitive density and orders, attribute values), which results in a chaotic and challenging-to-learn solution space.

To obtain consistently distributed Gaussian attribute sets for shrinking the solution space, we particularly develop a two-stage proxy ground-truth creation workflow, as depicted in Fig. 2. Given the task characteristics, we uniformly sample a dense 3D point cloud from the ground-truth human body surface to serve as the desired Gaussian positions  $\{\hat{\mathbf{p}}_j^{(n)}\}_{n=1}^N$ . The other four types of attributes (i.e., opacities, scalings, rotations, SHs) are deduced from two sequential processing stages of what we call *per-scene overfitting* and *distribution unification*, as introduced below.

1) *Stage 1: Per-Scene Overfitting*: This stage independently performs 3DGS overfitting on each of the  $J$  human captures, but with one subtle difference from the vanilla optimization scheme. Specifically, instead of directly maintaining Gaussian attributes as learnable variables, we introduce a point cloud learning network  $\mathcal{F}_1(\cdot; \Phi_1)$ , which consumes  $\{\hat{\mathbf{p}}_j^{(n)}\}_{n=1}^N$  at the input end and outputs the rest types of Gaussian attributes, as formulated below:

$$\{\bar{\alpha}_j^{(n)}, \bar{\mathbf{s}}_j^{(n)}, \bar{\mathbf{q}}_j^{(n)}, \bar{\mathbf{c}}_j^{(n)}\}_{n=1}^N = \mathcal{F}_1(\{\hat{\mathbf{p}}_j^{(n)}\}_{n=1}^N; \Phi_1). \quad (7)$$

The purpose of moving Gaussian attributes to the output end of a neural network is to exploit the inherent smoothness tendency [25] of the outputs of the neural network. Accordingly, for the  $j$ -th training sample, the per-scene optimization objective can be formulated as:

$$\bar{\mathcal{A}}_j = \{\hat{\mathbf{p}}_j^{(n)}, \bar{\alpha}_j^{(n)}, \bar{\mathbf{s}}_j^{(n)}, \bar{\mathbf{q}}_j^{(n)}, \bar{\mathbf{c}}_j^{(n)}\}_{n=1}^N, \quad (8)$$

$$\min_{\Phi_1} \sum_{k=1}^K \ell_{\text{pmet}}(\mathcal{R}(\bar{\mathcal{A}}_j; \mathcal{V}_j^{(k)}); \mathbf{I}_j^{(k)}),$$

where  $\ell_{\text{pmet}}$  involves both  $L_1$  and SSIM measurements. Additionally, auxiliary constraints are imposed over scaling and opacity attributes to suppress highly non-uniform distributions. The auxiliary constraints are as follows:

$$\sum_{n=1}^N \|\text{radius}(\bar{\mathbf{s}}_j^{(n)}) - \text{kdist}(\hat{\mathbf{p}}_j^{(n)})\|^2 + \sum_{n=1}^N \|\bar{\alpha}_j^{(n)} - 1\|^2, \quad (9)$$

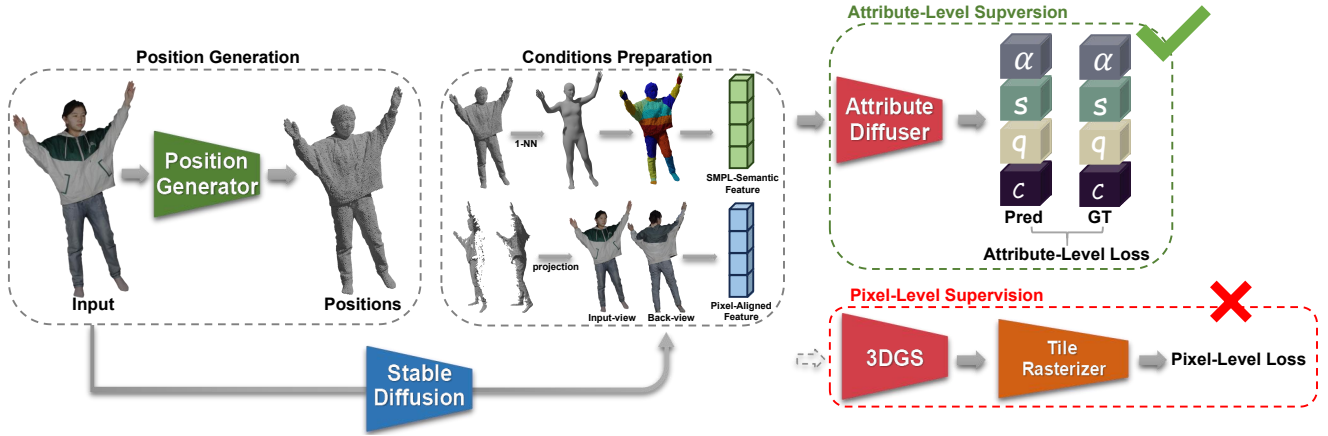


Fig. 3: The framework of our HuGDiffusion. HuGDiffusion predicts 3D Gaussian positions and a back-view image using a position generator and a stable diffusion module. It assigns SMPL semantic labels to points in 3D Gaussians, deducing an SMPL-semantic feature. The 3D Gaussians are decomposed for front- and back-view projection, achieving a pixel-aligned feature. Both features condition the 3D Gaussian attribute diffuser.

where  $\text{radius}(\cdot)$  and  $\text{kdist}(\cdot)$  are the operations to get the radiuses of the Gaussians and the mean distances between the Gaussians and their neighbors.

2) *Stage 2: Distribution Unification.*: Though the preceding stage has preliminarily deduced a dataset of Gaussian attribute sets  $\{\hat{\mathcal{A}}_j\}_{j=1}^J$ , the per-scene independent optimization can still lead to certain degrees of randomness and distribution inconsistency. Therefore, in the second stage, we introduce another deep set architecture  $\mathcal{F}_2(\cdot; \Phi_2)$  to overfit the whole  $J$  training samples:

$$\begin{aligned} \{\hat{\mathcal{A}}_j\}_{j=1}^J &= \mathcal{F}_2(\{\bar{\mathcal{A}}_j\}_{j=1}^J; \Phi_2), \\ \min_{\Phi_2} \sum_{j=1}^J \sum_{k=1}^K \ell_{\text{pmet}}(\mathcal{R}(\hat{\mathcal{A}}_j; \mathcal{V}_j^{(k)}); \mathbf{I}_j^{(k)}). \end{aligned} \quad (10)$$

Since it is impractical to feed all  $J$  training samples all at once, we adopt a batch-wise scheme with a certain number of training epochs, after which the resulting optimized  $\{\hat{\mathcal{A}}_j\}_{j=1}^J$  serves as our required proxy ground-truths.

#### D. Gaussian Attribute Diffusion

Having created a collection of proxy ground-truth Gaussian attributes  $\{\hat{\mathcal{A}}_j\}_{j=1}^J$  as supervision signals, we shift our attention to modeling the target distribution  $q(\mathcal{A}|\mathbf{I}_s)$  conditioned on the input single-view image  $\mathbf{I}_s$  to predict the desired Gaussian attribute set  $\mathcal{A}$ . First, we separately predict Gaussian positions, which is essentially a 3D point cloud. Second, we treat the obtained point cloud as geometric priors and extract human-centric features and then feed them into a conditional diffusion pipeline for diffusing the rest types of Gaussian attributes.

1) *Generation of Gaussian Positions.*: In the training phase of the generalizable human 3DGS framework, we directly use the Gaussian positions  $\{\hat{\mathbf{p}}_j^{(n)}\}_{n=1}^N$  prepared in the proxy ground-truth creation process. In the inference phase, we need to estimate the Gaussian positions from the input image. In our implementation, we design a position generator with the rectification of the SMPL parametric human model.

The position generator begins with monocular depth estimation [22] to generate from  $\mathbf{I}_s$  the corresponding depth map,

which is converted into a partial 3D point cloud. In parallel, we also estimate from  $\mathbf{I}_s$  the corresponding SMPL model, whose pose is further rectified by the partial point cloud. Then, we feed the rectified SMPL model and the partial point cloud into a point cloud generation network to output the desired set of 3D Gaussian positions. To ensure the uniformity of point cloud, we perform point cloud upsampling and then apply farthest point sampling. In this way, we can stably obtain a set of accurate 3D Gaussian positions  $\{\mathbf{p}^{(n)}\}_{n=1}^N$  as geometric priors.

2) *Extraction of human-centric Features.*: To supplement more informative conditioning signals for the subsequent attribute diffusion, we further extract two aspects of human-centric features.

The first is *pixel-aligned features* for providing visual appearance information. To achieve this, we project the 3D Gaussian positions onto the input image space. Then we utilize [1] to predict a back-view image  $\mathbf{I}_{\text{back}}$  with respect to the view of  $\mathbf{I}_s$ . The visible and invisible partitions of  $\{\mathbf{p}^{(n)}\}_{n=1}^N$  are respectively projected onto  $\mathbf{I}_s$  and  $\mathbf{I}_{\text{back}}$ , and the feature maps corresponding to  $\mathbf{I}_s$  and  $\mathbf{I}_{\text{back}}$  are extracted via 2D CNNs. Finally, we concatenate the visible and invisible pixel-aligned features to form the pixel-aligned feature  $\beta^{(n)}$ .

The second is *SMPL-semantic features* for strengthening the awareness of human body structure. We incorporate semantic labels defined on SMPL. We perform the nearest neighbor search to identify the nearest points of the 3D Gaussians on the SMPL surface. For each 3D Gaussian, we retrieve the nearest SMPL point index, distance, and semantic label, which are embedded into the latent space through MLPs. The resulting feature embeddings are concatenated to assign each point the SMPL-semantic feature  $\gamma^{(n)}$ .

3) *Conditional Diffusion.*: Having obtained Gaussian positions  $\mathbf{p}^{(n)}$ , pixel-aligned features  $\beta^{(n)}$ , and SMPL-semantic features  $\gamma^{(n)}$ , we perform condition diffusion to generate the rest attributes including  $\alpha^{(n)}$ ,  $\mathbf{s}^{(n)}$ ,  $\mathbf{q}^{(n)}$ , and  $\mathbf{c}^{(n)}$ . Empirically, we observe that simultaneously diffusing all these four types of attributes usually results in training collapse. We separate

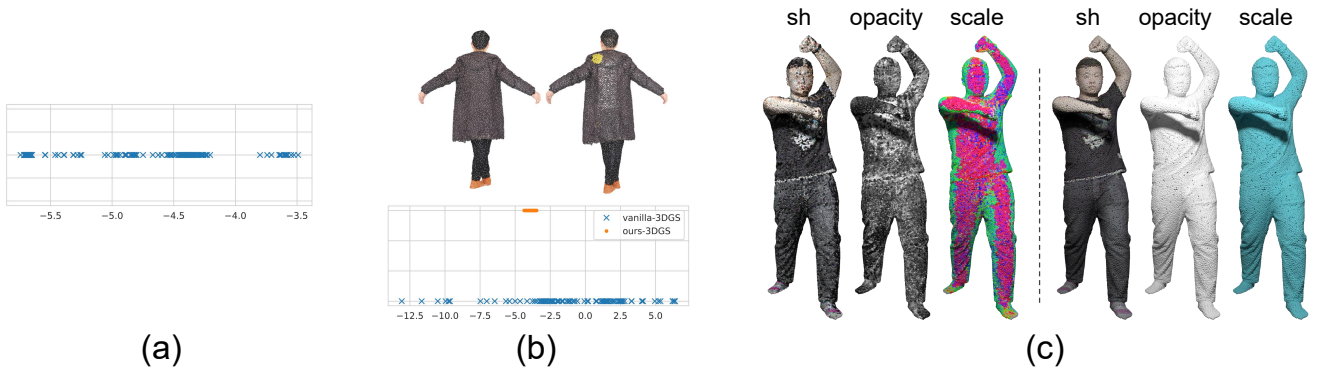


Fig. 4: (a) The large variation of vanilla-3DGS spherical harmonic values after 200 attempts on a scene. (b) Spherical harmonic values comparison of the local area (marked with yellow) between vanilla-3DGS and our proxy ground-truth 3D Gaussian attributes. (c) Visualization of spherical harmonic, opacity, and scale for vanilla-3DGS and our proxy ground-truth 3D Gaussian attributes. **Q** Zoom in for details.

the diffusion of SH coefficients from the other three types of attributes.

For training the generation of SH coefficients, we design an attribute diffuser  $\text{GSDIFF}_{\psi_1}$  to predict the noise at the given time step  $\mathbf{t}$  and use an  $L_2$  loss for supervision:

$$\begin{aligned} \epsilon^{(n)} &= \text{GSDIFF}_{\psi_1}(\tilde{\mathbf{c}}_t^{(n)}, \mathbf{p}^{(n)}, \beta^{(n)}, \gamma^{(n)}, \mathbf{t}), \\ \min_{\psi_1} \mathbb{E}_{\epsilon \sim \mathcal{N}} \|\hat{\epsilon}^{(n)} - \epsilon^{(n)}\|^2, \end{aligned} \quad (11)$$

where  $\tilde{\mathbf{c}}_t^{(n)}$  denote SH coefficients with noise added, and  $\hat{\epsilon}^{(n)}$  is the ground-truth noise. For inference, we sample random SH coefficients  $\mathbf{c}_T^{(n)}$  from the Gaussian distribution and iteratively remove noise to achieve  $\mathbf{c}_0^{(n)}$ . However, as demonstrated in PDR [16], the inductive bias of the evidence lower bound (ELBO) is unclear in the 3D domain, resulting in  $\mathbf{c}_0^{(n)}$  still containing noise, we further adopt an extra-step to remove the remaining noises. Also, we predict the other attributes, i.e.,  $\alpha^{(n)}, \mathbf{s}^{(n)}, \mathbf{q}^{(n)}$  at this extra-step.

$$\begin{aligned} \{\epsilon^{(n)}, \alpha^{(n)}, \mathbf{s}^{(n)}, \mathbf{q}^{(n)}\} &= \text{GSDIFF}_{\psi_2}(\mathbf{c}_0^{(n)}, \mathbf{p}^{(n)}, \beta^{(n)}, \gamma^{(n)}), \\ \mathbf{c}^{(n)} &= \mathbf{c}_0^{(n)} - \epsilon^{(n)}, \\ \min_{\psi_2} \|\mathbf{c}^{(n)} - \hat{\mathbf{c}}^{(n)}\|^2 + \|\alpha^{(n)} - \hat{\alpha}^{(n)}\|^2 + \\ &\|\mathbf{s}^{(n)} - \hat{\mathbf{s}}^{(n)}\|^2 + \|\mathbf{q}^{(n)} - \hat{\mathbf{q}}^{(n)}\|^2, \end{aligned} \quad (12)$$

Finally, we obtain a 3D Gaussian attribute set  $\{\mathbf{p}^{(n)}, \alpha^{(n)}, \mathbf{s}^{(n)}, \mathbf{q}^{(n)}, \mathbf{c}^{(n)}\}$  of a scene when given a single-view image  $\mathbf{I}_s$ , which can be used to render novel views of the human body.

#### IV. EXPERIMENTS

##### A. Datasets and Implementation Details

We utilized 480 human models from Thuman2 [42] for the construction of proxy ground truth 3D Gaussian attributes and the training of the attribute diffusion model. We quantitatively evaluated HuGDiffusion on Thuman2 (20 humans), CityuHuman (20 humans) [32], 2K2K (25 humans) [3] and CustomHuman (40 humans) [5]. We adopted the peak signal-to-noise ratio (PSNR), structural similarity index (SSIM),

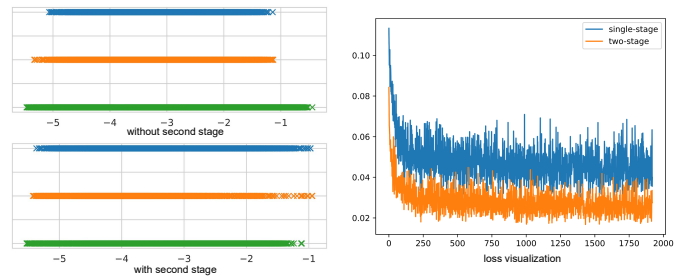


Fig. 5: The visualization of distributions and loss. **Q** Zoom in for details.

and Learned Perceptual Image Patch Similarity (LPIPS) as evaluation metrics.

When constructing the proxy ground truth 3D Gaussian attributes, we rendered 360 views for each human, and we uniformly sampled 20000 points from each human surface, which was the initial 3D Gaussian position. In the first stage, we utilized a Point Transformer as the backbone to predict the 3D Gaussian attributes. We overfitted the Point Transformer for 4000 epochs for each human subject, using the Adam optimizer with a learning rate of 0.0002. In the second stage, we employed another Point Transformer as the backbone. the batch size was set to 4, the number of epochs to 1300, and we continued using the Adam optimizer with a learning rate of 0.0002. Other settings of 3DGS followed [11]. To train HuGDiffusion, we designed the attribute diffusion model, with PointNet++ serving as the backbone<sup>1</sup>. ResNet18 with pre-trained weights was used to extract image features when preparing the pixel-aligned feature. During training, the batch size was set to 4, the number of epochs was set to 300, the optimizer was Adam, and the learning rate was 0.0002.

##### B. Analysis on 3D Gaussian Attribute Construction

We first conducted experiments to demonstrate why point transformers are necessary for overfitting and why a two-stage

<sup>1</sup>We found that the voxel size of the point transformer will seriously affect the performance. Hence, we did not use it as the backbone of HuGDiffusion.

TABLE I: Quantitative comparisons of different methods on Thuman, CityuHuman, 2K2K, and CustomHuman datasets. The best results are highlighted in **bold**.  $\uparrow$ : the higher the better.  $\downarrow$ : the lower the better.

Method	Metric	Thuman			CityuHuman			2K2K			CustomHuman		
		PSNR $\uparrow$	SSIM $\uparrow$	LPIPS $\downarrow$	PSNR $\uparrow$	SSIM $\uparrow$	LPIPS $\downarrow$	PSNR $\uparrow$	SSIM $\uparrow$	LPIPS $\downarrow$	PSNR $\uparrow$	SSIM $\uparrow$	LPIPS $\downarrow$
GTA [45]		25.78	0.919	0.085	27.41	0.923	0.075	24.15	0.921	0.080	28.86	0.920	0.088
SiTH [6]		25.36	0.919	0.083	29.21	0.934	0.067	24.30	0.920	0.076	26.47	0.911	0.095
LGM [31]		25.13	0.915	0.096	29.78	0.941	0.074	27.99	0.938	0.071	31.91	0.944	0.077
SHERF [8]		26.57	0.927	0.081	30.13	0.942	0.067	27.29	0.931	0.072	27.88	0.916	0.096
HuGDiffusion		<b>30.03</b>	<b>0.953</b>	<b>0.065</b>	<b>32.47</b>	<b>0.954</b>	<b>0.062</b>	<b>30.64</b>	<b>0.949</b>	<b>0.060</b>	<b>34.82</b>	<b>0.958</b>	<b>0.055</b>

TABLE II: The results of different settings on Thuman. Results: Ground truth point clouds are used. *Results: generated point clouds are used.*

	Pixel-Level	Attribute-Level		
		vanilla	neural	joint
PSNR $\uparrow$	31.84 (29.02)	FAIL	32.99 (29.53)	33.22 (29.71)
SSIM $\uparrow$	0.963 (0.953)	FAIL	0.968 (0.949)	0.971 (0.951)
LPIPS $\downarrow$	0.056 (0.070)	FAIL	0.052 (0.069)	0.048 (0.065)



Fig. 6: The visual comparison with vanilla-3DGS and point transformer at the first stage.  $\text{Q}$  Zoom in for details.

workflow is required.

**Defect of Vanilla-3DGS.** The solution space of vanilla-3DGS is expansive, primarily due to directly optimizing numerical values and the strong interdependency of its attributes. To validate this, we designed three experiments. Firstly, we fixed all random seeds in python, numpy and pytorch and optimized the 3DGS model on a specific scene 200 times. Subsequently, we plotted the results from 200 optimizations, obtained by summing the spherical harmonic values of each optimization, as depicted in Fig. 4(a). The results exhibit significant variation. Secondly, we selected a local area (marked in yellow) on a human body expected to have the same color; however, as illustrated in Fig. 4(b), the spherical harmonic values ranged widely from -12.5 to 6. Lastly, we visualized the spherical harmonic, opacity, and scale attributes in Fig. 4(c) left column, revealing that vanilla-3DGS produced highly chaotic results. Although vanilla-3DGS can achieve better rendering results, its inherent randomness and lack of regularity make it impractical for learning (as illustrated in Tab. II). Therefore, it is not suitable for constructing the proxy ground truth 3D Gaussian attributes.

**The Necessity of two-stage construction.** We visualized the results of the per-scene overfitting stage in Fig. 4 (b)

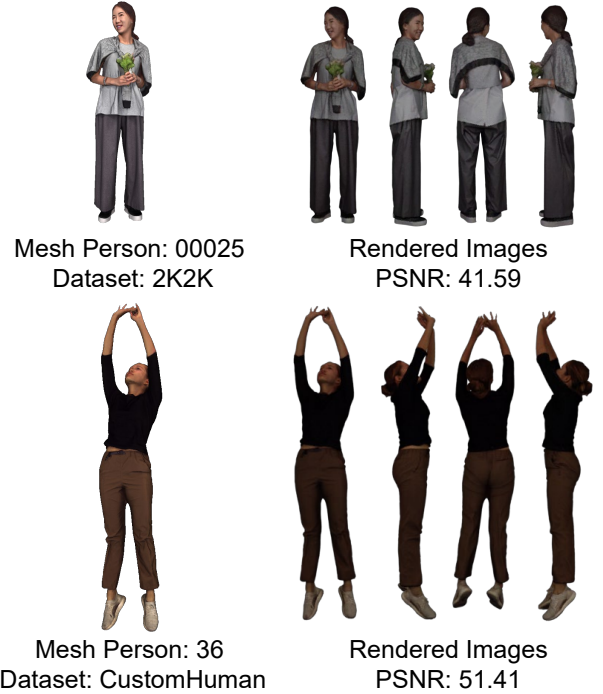


Fig. 7: The constructed results on 2K2K and CustomHuman datasets.  $\text{Q}$  Zoom in for details.

and (c) right column. Our point transformer-based 3DGS significantly reduced the variation range of spherical harmonic values in the local area, and the visualizations of the spherical harmonic, opacity, and scale attributes appeared cleaner and more uniform.

However, as depicted in Fig. 5, the 3D Gaussian attributes obtained from the first stage resulted in slow convergence during training, primarily due to the independent optimization of scenes, which caused distinct distributions across different scenes. After the second stage, the distribution among various scenes was better aligned, with the variances of the minimum and maximum values reduced from **0.0707** to **0.0329** and from **0.1114** to **0.1094**, respectively. As shown in Tab. II, the two-stage construction (**joint**) achieves better performance than the single-stage construction (**neural**).

We also directly applied the vanilla-3DGS in the first stage. However, the high level of randomness in the vanilla-3DGS could not be sufficiently mitigated by relying solely on the point transformer in the second stage, as illustrated in Fig.



Fig. 8: Visual comparisons of our method against GTA [45], SiTH [6], LGM [31], and Sherf [8].  Zoom in for details.

6. This further demonstrates the necessity of using the point transformer in the first stage. Hence, a two-stage construction process is essential.

**Generalizability to Other Datasets.** To validate the generalizability of our two-stage construction process, we applied it to the 2K2K and CustomHuman datasets. As illustrated in Fig. 7, the process consistently produced satisfactory results across these datasets.

### C. Comparisons with State-of-the-Art Methods

We compared our HuGDiffusion with four state-of-the-art methods: GTA [45], LGM [31], SiTH [6], and SHERF [8]. The four used datasets were collected from individuals of different ages, genders, and races. As reported in Tab. I, HuGDiffusion achieves the best quantitative performance across all metrics on all datasets, underscoring the effectiveness and generalization capability of HuGDiffusion.

GTA and SiTH suffer from the grid resolution of the marching cube and produce broken reconstructed human bodies,

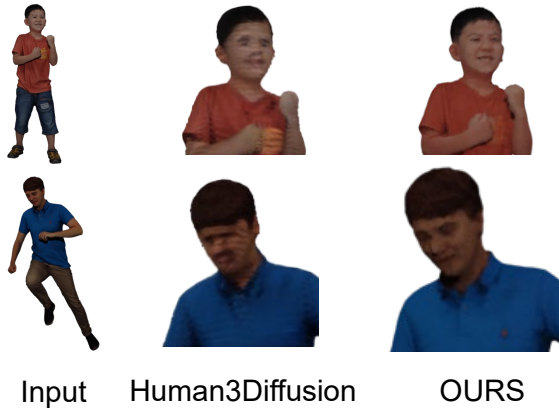


Fig. 9: Visual comparison with Human3Diffusion [39] and HuGDiffusion. 🔍 Zoom in for details.

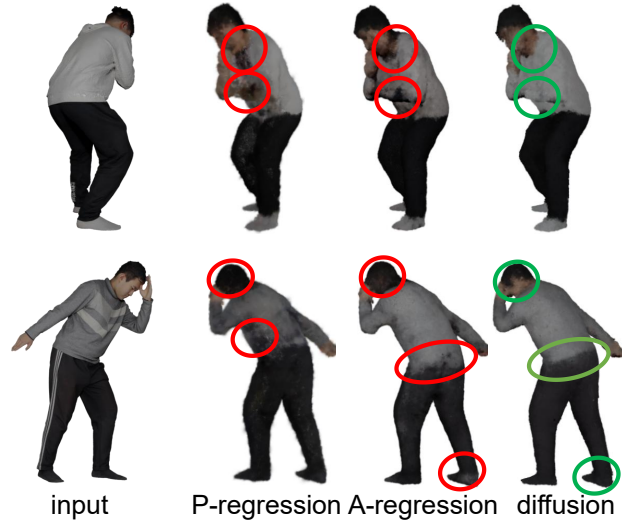


Fig. 11: Regression-based model v.s. diffusion-based model. P-regression: supervised with pixel-level signals. A-regression: supervised with attribute-level signals. 🔍 Zoom in for details.

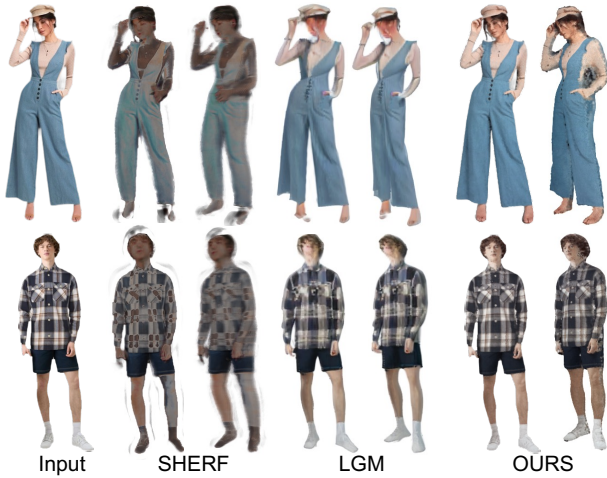


Fig. 10: The visual comparison with SHERF [8] and LGM [31] on the wild images. 🔍 Zoom in for details.

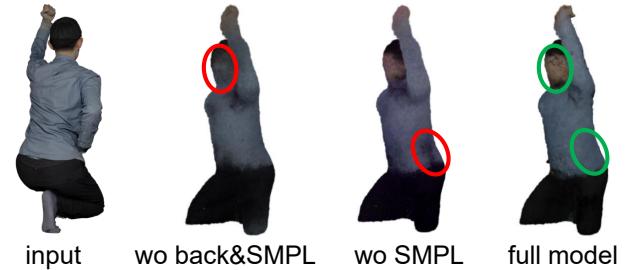


Fig. 12: Without occluded side image v.s. with occluded side image. 🔍 Zoom in for details.

resulting in low-fidelity novel views. Moreover, their results are usually in the wrong poses. However, as shown in Fig. 8, our HuGDiffusion is capable of rendering fine-grained input view images while maintaining texture consistency across different view directions with correct poses.

LGM is a generalizable 3DGS model that predicts the 3D Gaussian attributes from the multi-view generated images. However, it occasionally predicts incorrect occluded side images, and the rendered images have low resolution due to consistency issues across different views. Our HuGDiffusion solves the consistency problem by generating the 3D Gaussian position first. Moreover, owing to our diffusion-based framework, the rendered images are more realistic, compared to LGM. Human3Diffusion [39] is specifically trained on human data, we also compare it on Thuman (its inference code has a bug in rotation normalization, we manually fix the wrong rotation of each person.). Human3Diffusion achieves PSNR 27.06, SSIM 0.934 and LPIPS 0.079. HuGDiffusion still performs better than Human3Diffusion. And Human3Diffusion cannot preserve the details of the input images, as shown in Fig. 9.

SHERF frequently encounters challenges with incorrect poses in SMPL models. While the estimated SMPL models exhibit poses similar to the given view on the 2D image, their poses are frequently incorrect in the 3D space, and SHERF lacks a module to rectify the SMPL models in 3D space. Additionally, SHERF heavily relies on the SMPL model and is unable to render loose clothing, as illustrated in Fig. 10, where it fails to render the hems of the overalls for the first individual. Furthermore, SHERF directly utilizes the input view to extract image features, which leads to incorrect occluded side information prediction when the occluded side of the human is not symmetrical with the frontal view. Our designed 3D Gaussian position generator and pixel-aligned feature can tackle these issues.

In comparison to SHERF and LGM on wild images, as shown in Fig. 10, SHERF fails to recover accurate colors and produces incorrect poses, while also struggling to render loose clothing. LGM, on the other hand, recovers correct colors but cannot preserve face identity or texture details.

A geometric comparison of GTA, SiTH, LGM, and HuGDiffusion in Table III shows that, while HuGDiffusion does not prioritize 3D surface recovery, it still delivers the best performance in this regard.



Fig. 13: Without SMPL semantic features v.s. with SMPL semantic features  Zoom in for details.

TABLE III: Quantitative geometric comparisons of GTA, SiTH and HuGDiffusion. The best results are highlighted in **bold**.

Method	Metric	Thuman		2K2K	
		CD↓	P2S↓	CD↓	P2S↓
GTA [45]		1.151	1.145	1.436	1.398
SiTH [6]		0.976	1.040	1.383	1.569
LGM [31]		1.545	1.366	1.196	1.101
HuGDiffusion		<b>0.708</b>	<b>0.733</b>	<b>0.887</b>	<b>0.875</b>

Furthermore, we provide ground truth occupancy or SDF data for GTA and SiTH, and ground truth 3D Gaussian positions for HuGDiffusion to assess the effect of shape correctness, as shown in Table IV. Although ground truth data enhances GTA and SiTH, HuGDiffusion achieves even greater gains, showcasing its robustness.

We also refer reviewers to the *Supplementary Material* for the video demo<sup>2</sup>.

#### D. Ablation Studies

**Diffusion-based Model.** Diffusion models demonstrate superior capabilities in generating unseen appearances compared to regression models. Figure 11 provides two examples illustrating this advantage. While regression models can achieve fair numerical performance, as shown in Table V, they typically fail to accurately reconstruct appearances in occluded areas. For example, in the first example, regardless of whether pixel-supervised or attribute-supervised regression-based models are used, they generate excessive black coloration in the neck and arm areas. In contrast, the diffusion model produces accurate white coloration in these regions. Furthermore, in the second example, both regression-based models generate entirely black heads, which appear incorrect and unnatural, and fail to produce accurate boundaries for the tops and pants. In comparison, the diffusion model generates more realistic and natural appearances in occluded areas. These results highlight the significant advantages of diffusion models in addressing these challenges.

**Occluded Side Image.** The predicted occluded side image provides coarse information about unseen areas for HuGDiffusion. When the occluded side image is excluded, as illustrated in Fig. 12, HuGDiffusion fails to predict the correct facial identity, resulting in a decline in quantitative performance. These results demonstrate that the occluded side image significantly

TABLE IV: Quantitative comparisons of GTA, SiTH and HuGDiffusion when providing ground truth and predicted 3D shapes. The best results are highlighted in **bold**.

Method	Metric	Ground Truth Shape			Predicted Shape		
		PSNR↑	SSIM↑	LPIPS↓	PSNR↑	SSIM↑	LPIPS↓
GTA [45]		24.82	0.930	0.059	25.78	0.919	0.085
SiTH [6]		26.81	0.941	0.048	25.36	0.919	0.083
HuGDiffusion		<b>33.79</b>	<b>0.971</b>	<b>0.050</b>	<b>30.03</b>	<b>0.953</b>	<b>0.065</b>

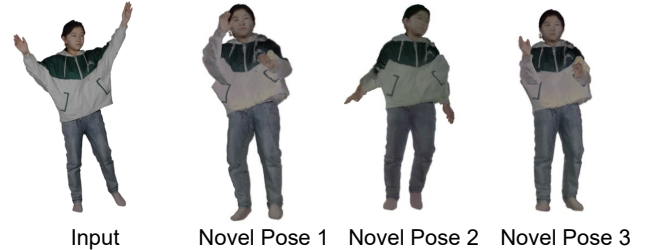


Fig. 14: Novel pose synthesis results of HuGDiffusion.  Zoom in for details.

contributes to enhancing the quality of predictions in unseen areas.

**SMPL Semantic Feature.** As presented in Fig. 13, when the SMPL semantic feature is not adopted, we observed that the boundary of the neck area became unclear, moreover, there are some red noisy pixels in the image. The absence of SMPL semantics constraints causes the network to lack clarity regarding the position of each point on the human body, leading to noisy rendering results and poor numerical performance.

**Novel Pose Synthesis.** We present several results of novel pose synthesis in Fig. 14. By blending the 3D Gaussian positions with the SMPL vertices and modifying the SMPL pose, we successfully achieve novel poses. Notably, the results are satisfactory despite the absence of a specifically trained model for this novel pose synthesis task.

#### E. Perceptual Evaluation

We conducted a Perceptual evaluation to compare various methods quantitatively. Specifically, we engaged 52 participants, including undergraduate students, postgraduate students from diverse research backgrounds, and industry professionals, to assess 8 different human bodies. For each human body, we presented three images generated by different methods and asked the participants to provide scores ranging from 1 to 5, reflecting the quality of the generated shapes. The rating scale was as follows: 1 - poor, 2 - below average, 3 - average, 4 - good, and 5 - excellent.

Fig. 15 shows the results of the subjective evaluation, including the overall scores, mean values, and standard deviations (std) of the scores. It can be observed that our HuGDiffusion achieves the highest mean score and the lowest std value.

<sup>2</sup><https://youtu.be/AVhfWnwP44>

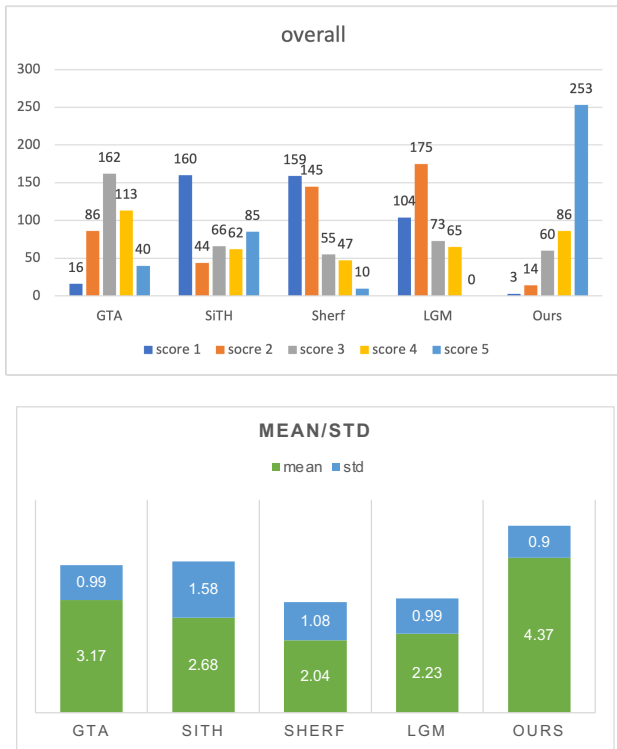


Fig. 15: Overall and mean/std results of the subjective evaluation.

TABLE V: The results of ablation studies on Thuman. R: regression-based model. D: diffusion-based model.

		Back Image	Smpl Semantic	PSNR $\uparrow$	SSIM $\uparrow$	LPIPS $\downarrow$
Pxlle-Level		✓	✓	29.02	0.953	0.070
Attribute-Level	R	✓	✓	29.71	0.951	0.065
	D	✗	✗	28.44	0.948	0.074
		✓	✗	29.63	0.950	0.070
		✓	✓	30.03	0.953	0.065

## V. CONCLUSION

We introduced HuGDiffusion, an innovative 3D Gaussian attribute diffusion framework for novel view synthesis from single-view human images. The approach employs a two-stage workflow to construct precise 3D Gaussian attributes, enabling a diffusion training process driven by attribute-level supervision. Utilizing a PointNet++-based architecture, the framework effectively denoises the 3D Gaussian attributes to generate accurate and plausible appearances for occluded areas. Additionally, human-centric features were integrated as conditions to enhance the training process. Extensive experimental evaluations reveal that HuGDiffusion consistently outperforms state-of-the-art methods across both quantitative metrics and qualitative assessments.

## REFERENCES

[1] Tim Brooks, Aleksander Holynski, and Alexei A Efros. Instructpix2pix: Learning to follow image editing instructions. In *Proc. CVPR*, pages 18392–18402, 2023.

[2] Xiangjun Gao, Jiaolong Yang, Jongyoo Kim, Sida Peng, Zicheng Liu, and Xin Tong. Mps-nerf: Generalizable 3d human rendering from multiview images. *IEEE TPAMI*, 2022.

[3] Sang-Hun Han, Min-Gyu Park, Ju Hong Yoon, Ju-Mi Kang, Young-Jae Park, and Hae-Gon Jeon. High-fidelity 3d human digitization from single 2k resolution images. In *Proc. CVPR*, pages 12869–12879, 2023.

[4] Xu He, Xiaoyu Li, Di Kang, Jiangnan Ye, Chaopeng Zhang, Liyang Chen, Xiangjun Gao, Han Zhang, Zhiyong Wu, and Haolin Zhuang. Magicman: Generative novel view synthesis of humans with 3d-aware diffusion and iterative refinement. *arXiv preprint arXiv:2408.14211*, 2024.

[5] Hsuan-I Ho, Lixin Xue, Jie Song, and Otmar Hilliges. Learning locally editable virtual humans. In *Proc. CVPR*, pages 21024–21035, 2023.

[6] I Ho, Jie Song, Otmar Hilliges, et al. Sith: Single-view textured human reconstruction with image-conditioned diffusion. In *Proc. CVPR*, pages 538–549, 2024.

[7] Jinhui Hou, Zhiyu Zhu, Junhui Hou, Hui Liu, Huanqiang Zeng, and Hui Yuan. Global structure-aware diffusion process for low-light image enhancement. In *Proc. NeurIPS*, 2024.

[8] Shoukang Hu, Fangzhou Hong, Liang Pan, Haiyi Mei, Lei Yang, and Ziwei Liu. SHERF: Generalizable human nerf from a single image. In *Proc. ICCV*, pages 9352–9364, 2023.

[9] Shoukang Hu, Tao Hu, and Ziwei Liu. Gauhuman: Articulated gaussian splatting from monocular human videos. In *Proc. CVPR*, pages 20418–20431, 2024.

[10] Wei Jiang, Kwang Moo Yi, Golnoosh Samei, Oncel Tuzel, and Anurag Ranjan. Neuman: Neural human radiance field from a single video. In *Proc. ECCV*, pages 402–418, 2022.

[11] Bernhard Kerbl, Georgios Kopanas, Thomas Leimkühler, and George Drettakis. 3d gaussian splatting for real-time radiance field rendering. *ACM TOG*, 42(4):139–1, 2023.

[12] Muhammed Kocabas, Jen-Hao Rick Chang, James Gabriel, Oncel Tuzel, and Anurag Ranjan. Hugs: Human gaussian splats. In *Proc. CVPR*, pages 505–515, 2024.

[13] Ruoshi Liu, Rundi Wu, Basile Van Hoorick, Pavel Tokmakov, Sergey Zakharov, and Carl Vondrick. Zero-1-to-3: Zero-shot one image to 3d object. In *Proc. ICCV*, pages 9298–9309, 2023.

[14] Tianqi Liu, Guangcong Wang, Shoukang Hu, Liao Shen, Xinyi Ye, Yuhang Zang, Zhiguo Cao, Wei Li, and Ziwei Liu. Fast generalizable gaussian splatting reconstruction from multi-view stereo. In *Proc. ECCV*, 2024.

[15] Shitong Luo and Wei Hu. Diffusion probabilistic models for 3d point cloud generation. In *Proc. CVPR*, pages 2837–2845, 2021.

[16] Zhaoyang Lyu, Zhifeng Kong, Xudong XU, Liang Pan, and Dahua Lin. A conditional point diffusion-refinement paradigm for 3d point cloud completion. In *Proc. ICLR*, 2022.

[17] Zhaoyang Lyu, Jinyi Wang, Yuwei An, Ya Zhang, Dahua Lin, and Bo Dai. Controllable mesh generation through sparse latent point diffusion models. In *Proc. CVPR*, pages 271–280, 2023.

[18] Luke Melas-Kyriazi, Christian Rupprecht, and Andrea Vedaldi. Pc2: Projection-conditioned point cloud diffusion for single-image 3d reconstruction. In *Proc. CVPR*, pages 12923–12932, 2023.

[19] Ben Mildenhall, Pratul P Srinivasan, Matthew Tancik, Jonathan T Barron, Ravi Ramamoorthi, and Ren Ng. NeRF: Representing scenes as neural radiance fields for view synthesis. In *Proc. ECCV*, pages 99–106, 2020.

[20] Jiteng Mu, Shen Sang, Nuno Vasconcelos, and Xiaolong Wang. Actorsnerf: Animatable few-shot human rendering with generalizable nerfs. In *Proc. ICCV*, pages 18391–18401, 2023.

[21] Jeong Joon Park, Peter Florence, Julian Straub, Richard Newcombe, and Steven Lovegrove. DeepSDF: Learning continuous signed distance functions for shape representation. In *Proc. CVPR*, pages 165–174, 2019.

[22] Suraj Patni, Aradhya Agarwal, and Chetan Arora. ECoDepth: Effective conditioning of diffusion models for monocular depth estimation. In *Proc. CVPR*, pages 28285–28295, 2024.

[23] Sida Peng, Yuanqing Zhang, Yinghao Xu, Qianqian Wang, Qing Shuai, Hujun Bao, and Xiaozei Zhou. Neural body: Implicit neural representations with structured latent codes for novel view synthesis of dynamic humans. In *Proc. CVPR*, pages 9054–9063, 2021.

[24] Charles Ruizhongtai Qi, Li Yi, Hao Su, and Leonidas J Guibas. Pointnet++: Deep hierarchical feature learning on point sets in a metric space. In *Proc. NeurIPS*, 2017.

[25] Nasim Rahaman, Aristide Baratin, Devansh Arpit, Felix Draxler, Min Lin, Fred Hamprecht, Yoshua Bengio, and Aaron Courville. On the spectral bias of neural networks. In *Proc. ICML*, pages 5301–5310, 2019.

[26] Barbara Roessle, Norman Müller, Lorenzo Porzi, Samuel Rota Bulò, Peter Kontschieder, Angela Dai, and Matthias Nießner. L3dg: Latent 3d

- gaussian diffusion. In *Proc. SIGGRAPH Asia*, pages 1–11, 2024.
- [27] Robin Rombach, Andreas Blattmann, Dominik Lorenz, Patrick Esser, and Björn Ommer. High-resolution image synthesis with latent diffusion models. In *Proc. CVPR*, pages 10684–10695, 2022.
- [28] Chitwan Saharia, Jonathan Ho, William Chan, Tim Salimans, David J Fleet, and Mohammad Norouzi. Image super-resolution via iterative refinement. *IEEE TPAMI*, 45(4):4713–4726, 2022.
- [29] Shunsuke Saito, Zeng Huang, Ryota Natsume, Shigeo Morishima, Angjoo Kanazawa, and Hao Li. Pifu: Pixel-aligned implicit function for high-resolution clothed human digitization. In *Proc. ICCV*, pages 2304–2314, 2019.
- [30] Shunsuke Saito, Tomas Simon, Jason Saragih, and Hanbyul Joo. Pifuhd: Multi-level pixel-aligned implicit function for high-resolution 3d human digitization. In *Proc. CVPR*, pages 84–93, 2020.
- [31] Jiayang Tang, Zhaoxi Chen, Xiaokang Chen, Tengfei Wang, Gang Zeng, and Ziwei Liu. Lgm: Large multi-view gaussian model for high-resolution 3d content creation. In *Proc. ECCV*, pages 1–18, 2024.
- [32] Yingzhi Tang, Qijian Zhang, Junhui Hou, and Yebin Liu. Human as points: Explicit point-based 3d human reconstruction from single-view rgb images. *arXiv preprint arXiv:2311.02892*, 2023.
- [33] Yating Tian, Hongwen Zhang, Yebin Liu, and Limin Wang. Recovering 3d human mesh from monocular images: A survey. *IEEE TPAMI*, 2023.
- [34] Arash Vahdat, Francis Williams, Zan Gojcic, Or Litany, Sanja Fidler, Karsten Kreis, et al. LION: Latent point diffusion models for 3d shape generation. In *Proc. NeurIPS*, pages 10021–10039, 2022.
- [35] Yunsong Wang, Tianxin Huang, Hanlin Chen, and Gim Hee Lee. Freesplat: Generalizable 3d gaussian splatting towards free-view synthesis of indoor scenes. In *Proc. NeurIPS*, 2024.
- [36] Chung-Yi Weng, Brian Curless, Pratul P Srinivasan, Jonathan T Barron, and Ira Kemelmacher-Shlizerman. Humannerf: Free-viewpoint rendering of moving people from monocular video. In *Proc. CVPR*, pages 16210–16220, 2022.
- [37] Yuliang Xiu, Jinlong Yang, Dimitrios Tzionas, and Michael J Black. ICON: Implicit clothed humans obtained from normals. In *Proc. CVPR*, pages 13286–13296, 2022.
- [38] Hongyi Xu, Thiemo Alldieck, and Cristian Sminchisescu. H-nerf: Neural radiance fields for rendering and temporal reconstruction of humans in motion. In *Proc. NeurIPS*, pages 14955–14966, 2021.
- [39] Yuxuan Xue, Xianghui Xie, Riccardo Marin, and Gerard Pons-Moll. Human 3diffusion: Realistic avatar creation via explicit 3d consistent diffusion models. In *Proc. NeurIPS*, 2024.
- [40] Fan Yang, Jianfeng Zhang, Yichun Shi, Bowen Chen, Chenxu Zhang, Huichao Zhang, Xiaofeng Yang, Jiashi Feng, and Guosheng Lin. Magicboost: Boost 3d generation with multi-view conditioned diffusion. *arXiv preprint arXiv:2404.06429*, 2024.
- [41] Alex Yu, Vickie Ye, Matthew Tancik, and Angjoo Kanazawa. pixelnerf: Neural radiance fields from one or few images. In *Proc. CVPR*, pages 4578–4587, 2021.
- [42] Tao Yu, Zerong Zheng, Kaiwen Guo, Pengpeng Liu, Qionghai Dai, and Yebin Liu. Function4d: Real-time human volumetric capture from very sparse consumer rgbd sensors. In *Proc. CVPR*, pages 5746–5756, 2021.
- [43] Bowen Zhang, Yiji Cheng, Jiaolong Yang, Chunyu Wang, Feng Zhao, Yansong Tang, Dong Chen, and Baining Guo. Gaussiancube: A structured and explicit radiance representation for 3d generative modeling. In *Proc. NeurIPS*, 2024.
- [44] Lvmin Zhang, Anyi Rao, and Maneesh Agrawala. Adding conditional control to text-to-image diffusion models. In *Proc. ICCV*, pages 3836–3847, 2023.
- [45] Zechuan Zhang, Li Sun, Zongxin Yang, Ling Chen, and Yi Yang. Global-correlated 3d-decoupling transformer for clothed avatar reconstruction. In *Proc. NeurIPS*, 2023.
- [46] Zechuan Zhang, Zongxin Yang, and Yi Yang. Sifu: Side-view conditioned implicit function for real-world usable clothed human reconstruction. In *Proc. CVPR*, pages 9936–9947, 2024.
- [47] Fuqiang Zhao, Wei Yang, Jiakai Zhang, Pei Lin, Yingliang Zhang, Jingyi Yu, and Lan Xu. Humannerf: Efficiently generated human radiance field from sparse inputs. In *Proc. CVPR*, pages 7743–7753, 2022.
- [48] Shunyuang Zheng, Boyao Zhou, Ruizhi Shao, Boning Liu, Shengping Zhang, Liqiang Nie, and Yebin Liu. Gps-gaussian: Generalizable pixel-wise 3d gaussian splatting for real-time human novel view synthesis. In *Proc. CVPR*, pages 19680–19690, 2024.
- [49] Zerong Zheng, Tao Yu, Yebin Liu, and Qionghai Dai. Pamir: Parametric model-conditioned implicit representation for image-based human reconstruction. *IEEE TPAMI*, 44(6):3170–3184, 2021.
- [50] Junsheng Zhou, Weiqi Zhang, and Yu-Shen Liu. Diffgs: Functional gaussian splatting diffusion. In *Proc. NeurIPS*, 2024.
- [51] Linqi Zhou, Yilun Du, and Jiajun Wu. 3d shape generation and completion through point-voxel diffusion. In *Proc. ICCV*, pages 5826–5835, 2021.

- [52] Zi-Xin Zou, Zhipeng Yu, Yuan-Chen Guo, Yangguang Li, Ding Liang, Yan-Pei Cao, and Song-Hai Zhang. Triplane meets gaussian splatting: Fast and generalizable single-view 3d reconstruction with transformers. In *Proc. CVPR*, pages 10324–10335, 2024.



**Yingzhi Tang** received his B.S. degree in Computer Science and M.S. degree in Information Engineering from Xidian University, Xi'an, China, in 2018 and 2021 respectively. Currently, he is a Ph.D. student (2021-present) under the Department of Computer Science, City University of Hong Kong, HKSAR. His research focuses on deep learning-based point cloud processing, 3D human reconstruction for various 3D vision tasks.



**Qijian Zhang** received the B.S. degree in Electronic Information Science and Technology from Beijing Normal University, Beijing, China, in 2019, and then the Ph.D. degree in Computer Science from City University of Hong Kong, Hong Kong SAR, in 2024. He is currently an applied researcher in the TiMi L1 Studio of Tencent Games, focusing on 3D generative models and AI for games.



**Junhui Hou** is an Associate Professor with the Department of Computer Science, City University of Hong Kong. He holds a B.Eng. degree in information engineering (Talented Students Program) from the South China University of Technology, Guangzhou, China (2009), an M.Eng. degree in signal and information processing from Northwestern Polytechnical University, Xi'an, China (2012), and a Ph.D. degree from the School of Electrical and Electronic Engineering, Nanyang Technological University, Singapore (2016). His research interests are multi-dimensional visual computing.

Dr. Hou received the Early Career Award (3/381) from the Hong Kong Research Grants Council in 2018 and the NSFC Excellent Young Scientists Fund in 2024. He has served or is serving as an Associate Editor for *IEEE Transactions on Visualization and Computer Graphics*, *IEEE Transactions on Image Processing*, *IEEE Transactions on Multimedia*, and *IEEE Transactions on Circuits and Systems for Video Technology*.